# Silicon Nanowires with High-k Hafnium Oxide Dielectrics for Sensitive Detection of Small Nucleic Acid Oligomers

**Brian R. Dorvel,[§,⊥,¶] Bobby Reddy, Jr.,[†,⊥,¶] Jonghyun Go,[∥] Carlos Duarte Guevara,[†,⊥] Eric Salm,[‡,⊥] Muhammad Ashraful Alam,[∥] and Rashid Bashir[†,‡,⊥,*]**

[†]Department of Electrical and Computer Engineering, [‡]Department of Bioengineering, [§]Department of Biophysics and Computational Biology, and [⊥]Micro and Nanotechnology Lab, University of Illinois at Urbana—Champaign, Urbana, Illinois 61801, United States and [∥]School of Electrical and Computer Engineering, Purdue University, West Lafayette, Indiana 47906, United States. [¶]These authors contributed equally to this work.

**ABSTRACT** Nanobiosensors based on silicon nanowire field effect transistors offer advantages of low cost, label-free detection, and potential for massive parallelization. As a result, these sensors have often been suggested as an attractive option for applications in point-of-care (POC) medical diagnostics. Unfortunately, a number of performance issues, such as gate leakage and current instability due to fluid contact, have prevented widespread adoption of the technology for routine use. High-k dielectrics, such as hafnium oxide ($HfO_2$), have the known ability to address these challenges by passivating the exposed surfaces against destabilizing concerns of ion transport. With these fundamental stability issues addressed, a promising target for POC diagnostics and SiNWFETs has been small oligonucleotides, more specifically, microRNA (miRNA). MicroRNAs are small RNA oligonucleotides which bind to mRNAs, causing translational repression of proteins, gene silencing, and expressions are typically altered in several forms of cancer. In this paper, we describe a process for fabricating stable $HfO_2$ dielectric-based silicon nanowires for biosensing applications. Here we demonstrate sensing of single-stranded DNA analogues to their microRNA cousins using miR-10b and miR-21 as templates, both known to be upregulated in breast cancer. We characterize the effect of surface functionalization on device performance using the miR-10b DNA analogue as the target sequence and different molecular weight poly-L-lysine as the functionalization layer. By optimizing the surface functionalization and fabrication protocol, we were able to achieve <100 fM detection levels of the miR-10b DNA analogue, with a theoretical limit of detection of 1 fM. Moreover, the noncomplementary DNA target strand, based on miR-21, showed very little response, indicating a highly sensitive and highly selective biosensing platform.

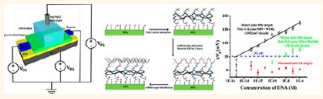

**KEYWORDS:** nanowire · miRNA · DNA · hafnium oxide · surface functionalization · sensing

Point-of-care (POC) diagnostics has emerged as an exciting field where devices can provide rapid, cheap, and accurate results in a portable format. Such diagnostic devices have the potential to provide critical patient information more rapidly at cheaper costs than instruments in centralized lab facilities, reducing the turnaround time for results in critical care situations.[1,2] Moreover, POC diagnostics can present patients with more control of their own therapy,[3] leading to greater patient satisfaction and improved clinical outcome.[4] In particular, treatment for various forms of cancer could benefit greatly from such POC devices. As our knowledge of cancer pathways rapidly grows, important indicators of cancer have been revealed, including changes in the genome, exome, transcriptome, and expression levels of several cancer biomarkers such as proteins and microRNA (miRNA). Devices that can rapidly detect cancer biomarkers in a rapid, accurate, multiplexed, and cost-efficient fashion would revolutionize cancer treatment, allowing for better evaluation of the efficacy of treatment, earlier detection of cancer, and deconvolution of the complex pathways that result in cancer.

Adaption of the ubiquitous field effect transistor (FET) technology has been proposed as a possible core technology for the sensing component of POC devices, due to the potential for low per unit cost, label-free detection, and amenability for scale-up and integration with signal processing electronics. Electrochemical detection methodologies based upon ion-sensitive field effect transistors (ISFETs) have been studied extensively,[5] including its use as biosensors (bioFET).[6−10] The performance of ISFET and bioFET relies on the charge of a binding biological analyte over the gate insulator of the FET, which induces changes in the source−drain current of the device. This allows for label-free, ultrasensitive, and rapid detection of relevant biological analytes.

Silicon nanowire FET devices (SiNWFETs), where the silicon channel has thicknesses and diameters in the tens of nanometers or less have further enhanced properties. Using SiNWFETs, researchers have demonstrated detection of biological analytes such as proteins,[11−16] DNA,[17−20] RNA,[21] ions,[22]

* Address correspondence to rbashir@illinois.edu.

Received for review April 5, 2012 and accepted June 13, 2012.

**Published online** 10.1021/nn301495k

and other small molecules[23] down to femtomolar concentrations. The increased sensitivity of these devices is mainly attributed to the increased gate control of the silicon channel due to a higher surface area to volume ratio. Thus, silicon nanowires show promise in cancer diagnosis since various cancer biomarkers may exist in small concentrations throughout the disease pathogenesis. Silicon nanowire FETs fabricated with "top-down" techniques[17,24−30] are particularly attractive, due to CMOS compatibility and high amenability for scale-up. However, though nanowire technology has existed for over a decade, several issues have prevented the technology from maturation into fully fledged POC products. Various issues have arisen regarding device stability in fluid such as measurement drift,[31] leakage paths through the sensing dielectric, high background $1/f$ noise,[32−34] and lack of repeatability. Silicon oxide, the traditional top gate dielectric, is one of the main culprits behind several of these issues, due to its relatively low dielectric constant, low pH buffering capacity, and susceptibility of gradual charge incorporation by ion diffusion when exposed to fluid.[35,36] To circumvent some of these issues, researchers have turned to high-k materials, including aluminum oxide ($Al_2O_3$),[37] hafnium oxide ($HfO_2$),[38] and tantalum oxide ($Ta_2O_5$).[39] High-k materials enable high gate oxide capacitance values even with physically thicker gate oxides, allowing a reduction in leakage current. $HfO_2$ has arisen as a particularly promising dielectric for ISFETs and MOSFETs due to its stability on silicon and its acceptable band gap and conduction band offset values. It can be deposited by chemical vapor deposition and yields improved pH sensitivity.[40,41]

To date, however, there have been very few reports that offer detailed characterization and application of hafnium oxide-based FETs for biosensing applications. Annealing of $HfO_2$ has been shown to improve pH sensitivity in a two-terminal EIS (electrolyte−insulator−semiconductor) capacitor using capacitance−voltage curves.[42] However, such a structure does not take advantage of the main desirable property for a FET, its intrinsic high current gain (high transconductance). In addition, $HfO_2$ deposited at high CVD temperatures for ISFETs leads to leakage paths in the silicon in high aspect ratio areas and results in higher roughness,[43] which is undesirable for a charge-based biosensor. The demonstrated sensitivity for this structure was very low (biotin and streptavidin detected down to ~50 $\mu$g/mL).[44] The pH sensing has been demonstrated with a FET structure with encouraging near-Nernstian results, but no molecular sensing has been reported to date.[38]

Here we describe a process for fabricating robust $HfO_2$-based silicon nanoFET sensors for biological applications. We use atomic layer deposition (ALD) to form the hafnium oxide dielectric and a wet-etch-based process for releasing the device structures. Unlike CVD methodologies, ALD is more conformal and can be performed at lower deposition temperatures with better process control. Additionally, the wet-etch-based process for device release eliminates the possibility of RIE-induced damage to the delicate dielectric layer. We have characterized in detail the properties of this low-temperature deposition process and optimized subsequent annealing conditions to create a high-quality dielectric. Moreover, we discuss the electrical and chemical advantages of the process, which include $HfO_2$ becoming an excellent wet etch stop for acid, alkali, and oxidizing chemistries. By thoroughly characterizing the $HfO_2$−silicon interface, we were able to produce a high-quality gate dielectric layer, resulting in a device with high repeatability and low hysteresis in fluid. The devices are highly stable and robust and show minimal drift over hours in fluid. As a result, we were able to achieve ~56 mV/pH unit response for nanowire devices. We then demonstrate the sensitive detection of a DNA analogue sequence of microRNA, which can be highly important cancer biomarkers. MicroRNAs (miRNAs) are small RNA oligonucleotides which bind to mRNAs, causing translational repression of proteins and gene silencing. In this work, we focus on sensing DNA analogues of miRNAs, with templates based upon miR-10b and miR-21, miRNAs commonly upregulated in breast cancer.[45−49] Moreover, miR-21 is found in a 4-fold higher concentration than miR-10b in normal tissue,[50] making miR-10b a harder analyte to detect even when upregulated. The devices were functionalized with different molecular weight polylysine strands and DNA probes specific to the miR-10b DNA analogue sequence. Different sensitivities for the different molecular weight polylysines were achieved for miR-10b, with lower sensitivity being achieved on the higher molecular weight polymer. Analysis of the layers showed lower probe density and higher roughness for the higher molecular weight layer of poly-L-lysine. The devices were able to achieve 100 fM detection limits for the miR-10b DNA in comparison against a miR-21 noncomplementary target, with a theoretical limit of detection of 1 fM. Various characteristic features of these systematic set of experiments are interpreted and supported by well-calibrated theoretical models.

## RESULTS AND DISCUSSION

One of the most important components of any silicon-based FET is the gate dielectric and its interface with silicon. We chose $HfO_2$ because it currently satisfies the requirements demanded for CMOS integration. Atomic layer deposition was chosen as the method for forming the gate dielectric because of its self-limiting growth process, meaning the thickness is controlled by the number of deposition cycles, allowing accurate thickness control and uniform step coverage. Moreover, due the reactive nature of the precursors, the

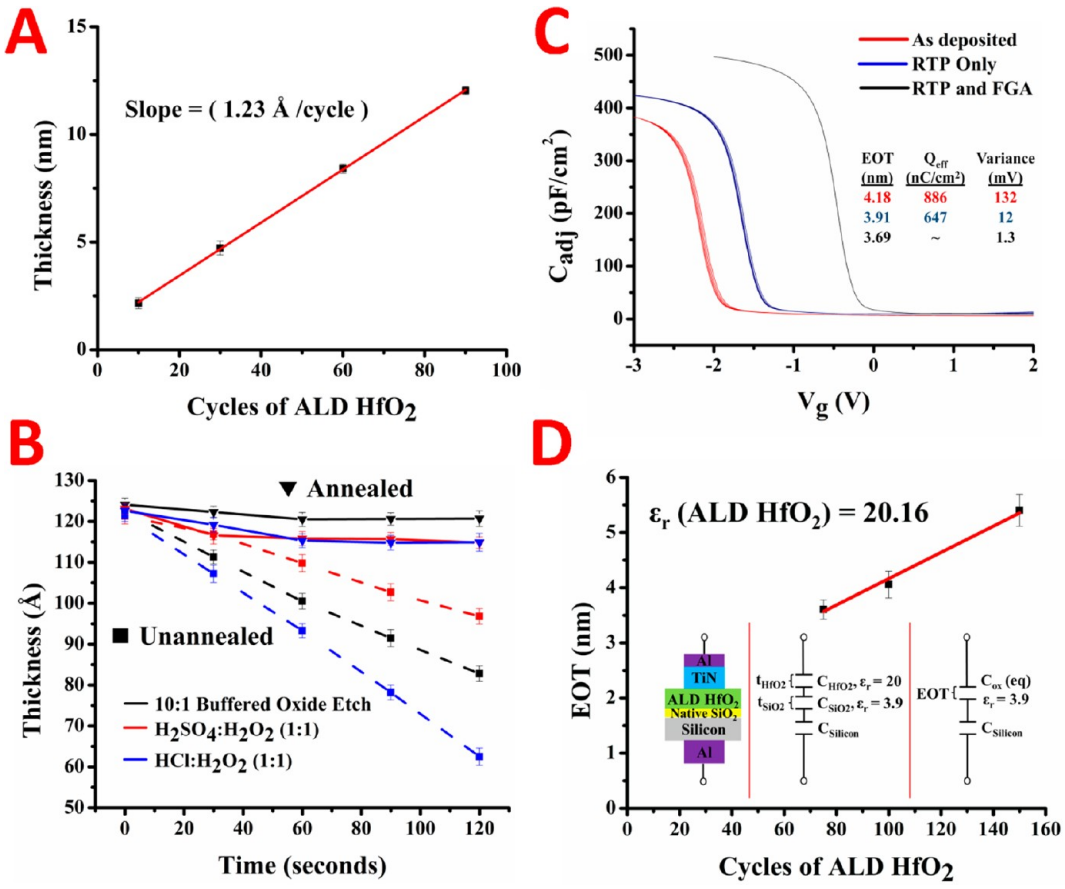


**Figure 1. Characterization of the $HfO_2$ gate dielectric deposited by atomic layer deposition. The thickness of $HfO_2$ *versus* the amount of ALD cycles is shown (A) with the slope inset. The effect of annealing the $HfO_2$ against chemical etchants is shown (B) with the ellipsometric thickness *versus* etching time. High-frequency capacitance−voltage curves for varying steps in the annealing procedure (C) with extracted values inset. The equivalent oxide thickness extracted from the *C*−*V* analysis *versus* the ALD cycle amount (D) with the extracted dielectric constant inset.**

temperature window for deposition is wide. However, the electrical and chemical properties of the film are temperature-dependent, as well. Before using $HfO_2$ as our gate dielectric, we characterized the properties of the hafnium oxide layer as deposited and how the thermal treatments taken during our process affect the gate dielectric.

During the nanowire fabrication process, the hafnium oxide must be amenable to hydrofluoric acid wet etching in order to create the contact vias over the source−drain regions of the FET. The concentration of HF also must be gentle enough as to not deteriorate the photoresist, leading us to use a 10:1 buffered oxide etchant (BOE) as the reagent. During the course of characterization, we observed that ALD deposition temperatures >200 °C resulted in a layer which would not etch in BOE solution. Layers deposited at <80 °C etched very quickly and had deposition rates much larger than the limiting rate of ~1 Å/cycle. In our process, we use a temperature of 120 °C, which gave us a good compromise between etching rate and deposition rate.

The characterization of the deposition thickness *versus* number of cycles was done using ellipsometry and is shown in Figure 1A. Here we assumed a simple bilayer stack of $HfO_2$ and Si, with refractive indices taken from the Sopra Material Library. By depositing ALD films between 10 and 90 cycles and measuring the thickness, we were able to verify the deposition rate per cycle and estimate the interfacial oxide thickness. The overall thickness ($T$) of the film on silicon is related to the $HfO_2$ deposition cycle number ($N_{HfO_2}$) by

$$T\ (\text{nm}) = R_{dep}N_{HfO_2} + t_{SiO_2}$$

where $R_{dep}$ is the deposition rate and $t_{SiO_2}$ is the native oxide thickness. By fitting a line to the data in Figure 1A, we get a deposition rate of 1.23 Å per cycle and, if we extrapolate back to zero cycles, a native oxide thickness of 9 Å. These results are within range of the reported growth rates of $HfO_2$[51,52] and thickness of a chemically grown native oxide.[53]

After ALD of the hafnium oxide films, we investigated how annealing would affect the chemical and electrical properties of the gate dielectric. Annealing of the films is an important parameter in optimizing the electrical performance of the gate dielectric. $HfO_2$ begins to crystallize at temperatures >500 °C, and the crystallization temperature is thickness-dependent,

increasing with decreasing thickness.[54] Crystallization, although helps increase the dielectric constant, is known to increase the leakage current through grain boundaries in MOS structures, as well. Thus, leakage would be amplified even more in an aqueous setting where ions are even more mobile than with a top metal. During our process, we decided to keep our anneal steps below 500 °C in order to avoid excess leakage affects. First, we perform a rapid thermal process in Ar at 500 °C for 60 s to densify the gate dielectric. Then, after the deposition of the leads, we do a forming gas anneal (Ar/10%$H_2$) at 450 °C for 30 min to passivate interface traps and anneal the leads. This constitutes our basic annealing procedure on the gate dielectric.

To examine how the anneal steps affected the gate dielectric chemically, we subjected the annealed and unannealed films to various strong acid etchants such as acid piranha and SC2, as well as in 10:1 BOE. The etch rates for hafnium oxide annealed *versus* unannealed are presented in Figure 1B. The films deposited at 120 °C show etch susceptibility for all etching solutions. Etch rates between 15 and 40 Å per minute are achieved with the various etching parameters. After the rapid thermal anneal and forming gas treatments, the hafnium oxide becomes chemically inert. The ellipsometric thickness of the films only changes by ~5 Å for each of the etchants. We attribute the thickness change to a thin carbonaceous layer on top of the film which is subsequently removed during exposure to the etching solutions.

In order to determine how the annealing affects the system electrically, MOS capacitors were formed by sputtering 30 nm TiN then 100 nm Al on the $HfO_2$ and 100 nm Al on the back of p-type silicon contact to create a capacitor with a structure shown in Figure 1D. High-frequency capacitance−voltage curves were taken for as-deposited, RTP only, and RTP+forming gas $HfO_2$ substrates. The results for a 100 cycle ALD $HfO_2$ film are shown in Figure 1C. Each device was swept 10 times to give insight into its stability. Using the high-frequency capacitance, we can extract parameters such as the oxide thickness, dielectric constant, effective charge, and flatband voltage. For a p-type MOS-C, the accumulation region of the $C-V$ curve is observed when negative voltages are applied to the gate. The oxide capacitance ($C_{ox}$) is the high-frequency capacitance when the device is biased for strong accumulation. If we assume the oxide is one entity, MOS-C acts like a single parallel-plate capacitor and $C_{ox}$ is related to the total oxide thickness ($t_{ox}$) by

$$C_{ox} = \frac{\varepsilon_0 K_{eff} A}{t_{ox}}$$

where $\varepsilon_0$ is the permittivity of free space, $A$ the capacitor area, and $K_{eff}$ the relative dielectric constant. From Figure 1C, we can see that $C_{ox}$ increases as we perform the annealing procedures, indicating that $K_{eff}$ is increasing and thus producing a higher quality $HfO_2$ layer. As we anneal the samples, we also notice the flatband voltage of the MOSCaps shifts to more positive potentials and the drift (or variance) becomes minimized for the RTP and forming gas system. The flatband voltage ($V_{fb}$) for MOSCaps can be expressed as

$$V_{fb} = \phi_{MS} - \frac{Q_{eff}}{C_{ox}}$$

where $\phi_{MS}$ is the work function difference between the metal and the semiconductor and $Q_{eff}$ is the effective oxide charge density, given by the sum of the oxide fixed charge ($Q_F$), oxide mobile charge ($Q_M$), and oxide-trapped charge ($Q_{OT}$) with $Q_{eff} = Q_F + Q_M + Q_{OT}$. We extract the flatband voltage from the flatband capacitance by interpolating between the closest voltages around the flatband capacitance value. We then extract the variance and $Q_{eff}$ for each MOSCap under study from the flatband voltages for each curve. The $Q_{eff}$ and variances for each of the anneals are found in the inset in Figure 1C. By annealing the substrates, we eliminate most of the effective charge and variance in the system. This is probably due to the removal of dangling bonds in the oxides and passivation of interface traps at the $HfO_2-SiO_2$ and $SiO_2-Si$ interfaces.[55]

To determine the dielectric constant of the annealed $HfO_2$, different cycle amounts of $HfO_2$ were deposited and $C_{ox}$ was determined. If we assume the dielectric is composed entirely of $SiO_2$ (since the dielectric constant is known), we can replace the $K_{eff}$ in eq 1 with the dielectric constant of $SiO_2$ (3.9) and extract an equivalent oxide thickness (EOT) for the layer. An example of this is found in the inset of Figure 1D, along with the stack for the MOS capacitors. The EOT of the $HfO_2$ MOSCaps was plotted *versus* the ALD cycle number ($N$) and is shown in Figure 1D. The EOT is a combination of the $HfO_2$ thickness and dielectric constant with the interfacial oxide thickness and dielectric constant. It can be expressed in a linear form by

$$\mathrm{EOT}(N) = \left(\frac{3.9}{K}\right) R_{dep} N + t_{SiO_2}$$

The dielectric constant can be extracted from the slope of the line $(3.9/K)R_{dep}$ assuming the deposition rate is known, which we extracted from ellipsometry. The interfacial oxide thickness is equivalent to the $y$-intercept of the line or by extrapolating the fit back to zero cycles. By fitting the points in Figure 1D, we determine a dielectric constant of 20.1 for the deposited ALD film, which meets expectations for a high-quality ALD $HfO_2$ film.[56] The extrapolated interfacial oxide thickness is ~17 Å, which agrees well with literature.[57] This value is substantially higher than the extracted value from ellipsometry of ~9 Å. We attribute this to the high diffusivity of oxygen in $HfO_2$, which

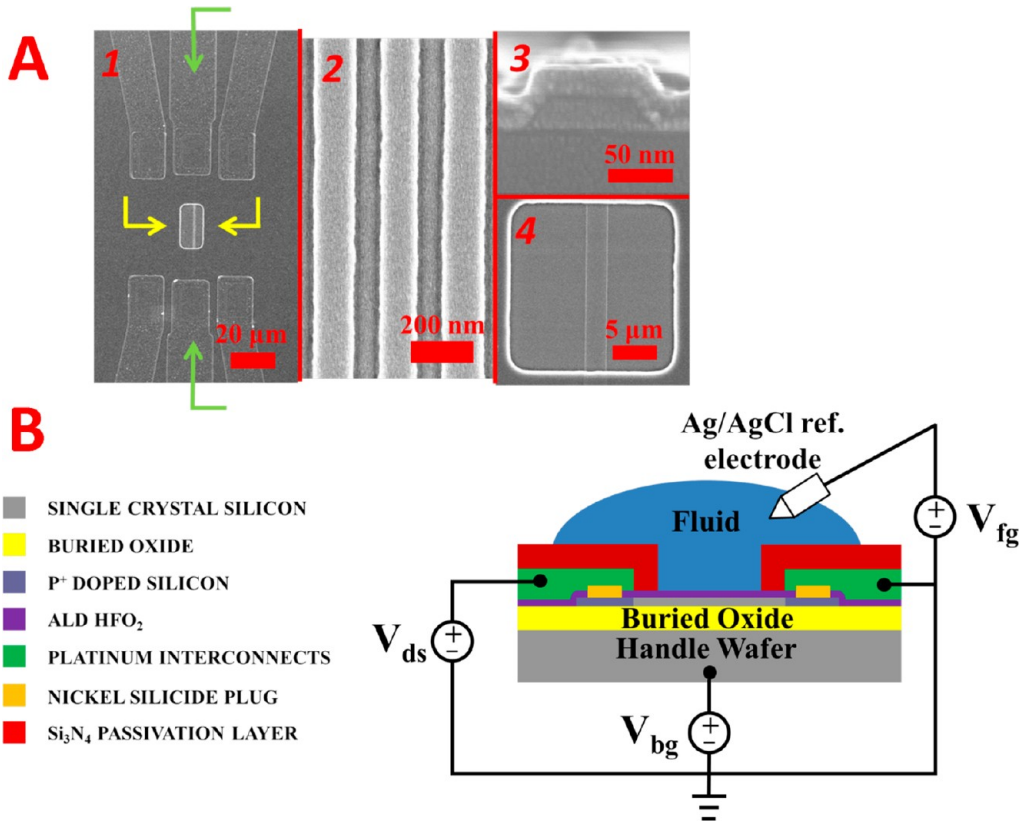


**Figure 2. (A) Scanning electron micrographs of the silicon nanowires. Image 1 shows an overview of the nanowire sensing area, with the source−drain metal leads (green arrows) and release window (yellow arrows) highlighted. A high-magnification top-down image of the nanowires is shown in 2. A cross-sectional image of a nanowire is in 3, while a top-down image of a nanoplate is in 4. (B) Horizontal cross-sectional schematic of sensing setup. The relevant structures are color-coded to the left, with an example electrical measurement setup for the source−drain ($V_{ds}$), fluid gate ($V_{fg}$), and back gate ($V_{bg}$).**

commonly increases the interfacial oxide thickness during anneals.[58,59]

Top-down and cross-section SEM images of the nanowires and nanoplates are shown in Figure 2A. Part 1 of Figure 2A shows an overall top down image of the nanowires. The release window is in the center (highlighted by the yellow arrows), while the metal leads connecting to the nanowires is highlighted by a green arrow. A high-magnification image of the nanowires in (1) is shown in Figure 2A(2), where the brighter areas represent the silicon nanowires. The nanowires appear to be ∼150 nm in width from the top-down image in (2), but the cross section in (3) shows them to be ∼100 nm wide. The cross section in (3) shows the trapezoidal nature of the nanowires from the TMAH anisotropic etch, as well as the surrounding $HfO_2$ gate dielectric. The thickness of the $HfO_2$ is approximately 13 nm from the image, although it is hard to measure it precisely due to the grain size of the metal sputtering. This thickness agrees well with the thickness information obtained from Figure 1. A top-down image for a nanoplate inside the release window is in (4) and shows a nanoplate of ∼2 $\mu$m width.

A schematic showing the full cross section of a nanowire and the setup for device testing is in Figure 2B. For fluid testing, a leak-free Ag/AgCl reference electrode is biased and swept, with a constant source−drain bias applied. A leak-free reference electrode was chosen since the salt solution encasing the electrode remains constant, helping to minimize drift of the electrode potential during measurements. Incorporating a steady reference electrode is critical in achieving stable measurements with high signal-to-noise ratio for FET sensing and has been discussed in literature previously.[60,61] The back of the handle wafer is grounded and the $I_d-V_g$ transfer curve measured.

The stability of the device under operation in 0.02× SSC buffer is shown in Figure 3. $I_d-V_g$ curves were swept from positive to negative bias with the Ag/AgCl electrode and cycled five times, shown in Figure 3A. The subthreshold slope extracted for the device is 112 mV/decade, comparatively on the low end for nanowire devices in fluid testing. Detailed numerical simulations were performed to validate experiment data (transfer characteristics in Figure 3A) and to further explore the sensitivity of our devices for pH sensing. In this numerical model, we solve the nonlinear Poisson−Boltzmann electrostatics for the sensor system (see Materials and Methods section for details). The simulation in Figure 3B shows that our detailed numerical simulation interprets the experimental results (red circles) consistently from subthreshold to superthreshold

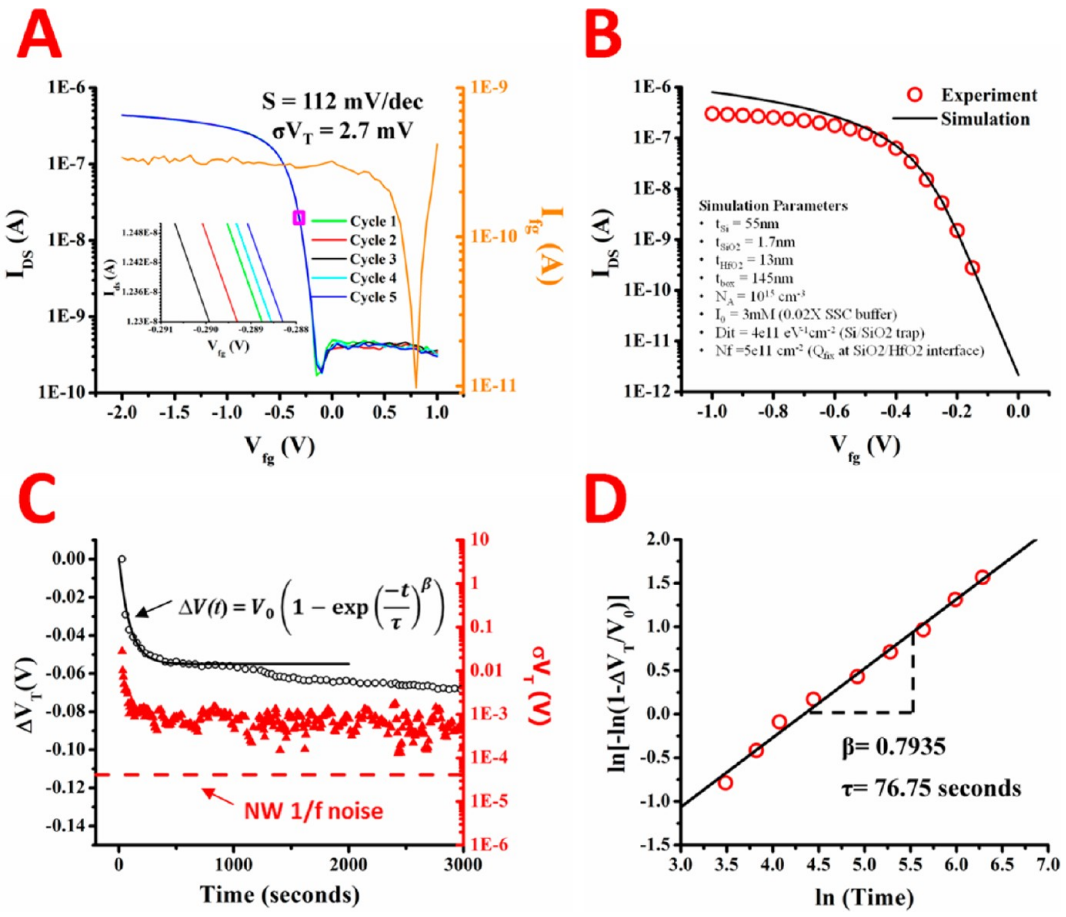


**Figure 3. (A) Representative source−drain current *versus* fluid gate voltage for a nanowire. The nanowires were swept for five cycles with the fluid gate leakage also measured (right side of graph), and an enlarged view of the curve repeatability is shown in the inset. The numerical simulation (black line) of the average of the experimental transfer curves (A) (red circles) is shown in (B) with the simulation parameters (inset). (C) Change in the threshold voltage (left side) and standard deviation in threshold (right side) *versus* time for a nanowire. The equation for modeling the gate voltage instability is shown in the inset, with the fit to the experimental data represented as the black line. The theoretically estimated low-frequency voltage noise is represented as a dashed red line. The experimental $\Delta V_t$ data were rearranged according to the equation to extract the time constant and dispersion parameter. (D) Natural log of the rearrangement is plotted *versus* the natural log of the time (red circles), with the linear fit to the data (black line) and the extracted parameters (inset).**

regime. The simulations accurately reproduce experimental transfer curves with the following parameters: interface trap densities ($D_{it}$) of $4 \times 10^{11}$ cm$^{-2}$ eV$^{-1}$, and fixed (negative) charge located at the $SiO_2/HfO_2$ interface with a density of $\sim 5 \times 10^{11}$ cm$^{-2}$. These values of interface trap density are consistent with widely accepted density of dangling Si bonds at the unpassivated $Si/SiO_2$ interface, and the estimate of fixed trap density is also consistent with those reported in literature.[62]

The standard deviation for threshold voltage on the devices is 2.7 mV. The combination of a low standard deviation and a low subthreshold slope indicate the combination of a high stability device and low drift reference electrode in electrolytic solutions. Moreover, the fluid is exposed to a $\sim 0.2$ cm$^2$ area on the chip, which if not passivated properly would cause leakage current much higher than the measured device current. The leakage throughout this area ranged from 300 pA to 1 nA, or 1.5 to 5 nA/cm$^2$. An example of long-term device stability in 0.02× SSC buffer is shown in Figure 3C. The threshold voltage after each sweep and the time were recorded and repeated over an hour. The change in threshold voltage over time decreases rapidly for the first 10 min, then stabilizes. The overall change is 65 mV/h, with only 10 mV change happening after the first 10 min. In planar ISFETs, the gate voltage instability can be described by a stretched exponential that is characteristic of dispersive transport in disordered materials expressed by

$$\Delta V_T(t) = \Delta V_{T_\infty}\left(1 - \exp\left(\frac{-t}{\tau}\right)^{\beta}\right) \quad (1)$$

where $\Delta V_{T_\infty}$ is the maximum $V_T$ change, $\tau$ is the time constant, and $\beta$ is the dispersion parameter that takes a value between $0 < \beta < 1$. As shown in Figure 3C, the theoretical fits according to this model (eq 1) agree well with the experimental data. By rearranging eq 1 and plotting the natural logarithm *versus* the natural log of time (Figure 3D), we are able to extract the time

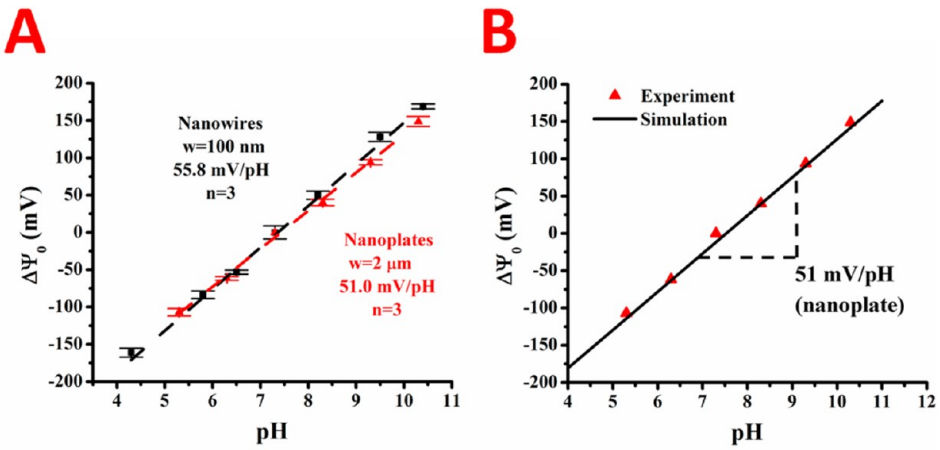


**Figure 4. (A) Change in surface potential of the $HfO_2$ sensing dielectric *versus* solution pH for nanowires (black) and nanoplates (red). The pH sensitivity for nanowires and nanoplates was extracted through linear regression and is displayed in the inset. (B) Numerical simulations (black line) of the nanoplate data (red triangles) using self-consistent Poisson−Boltzmann electrostatics and an OH group site binding model, with the extracted pH sensitivity shown in the inset.**

constant ($\tau$) and the dispersion parameter ($\beta$), which are also inset in Figure 3D. The values for $\Delta V_{T_\infty}$, $\beta$, and $\tau$ are 55 mV, 0.7935, and 76.75 s, respectively. The standard deviation of the device over five sweeps surrounding each time point was also plotted. Briefly, the standard deviation for sweep 15 would include points from sweeps 13−17. The standard deviation shows a ~1 mV standard deviation per five sweeps over the period of the hour. As the device equilibrates, the standard deviation between sweeps goes down. The solid red line indicates the theoretically estimated voltage noise of SiNW pH sensor composed of low-frequency noise and electrolyte noise (see Materials and Method section for the details), showing that the sensitivity is limited by the noise from measurement instrument (red triangles) not by the device's intrinsic noise. The leakage to the fluid gate, plotted over the course of an hour, stays relatively stable near 800 pA (see Supporting Information Figure S1). This indicates little degradation to the $HfO_2$ dielectric or passivation layer over that time period.

The response and stability of the devices to changes in pH was demonstrated using Robinson buffers for the nanowires and nanoplates. The changes in pH will cause a change in the surface potential on the device due to the proton reactive groups on top of the $HfO_2$ surface. Robinson buffer solutions ranging from pH values of 4.3−10.5 were used and the threshold voltages of nanowires and nanoplates extracted from the $I_d-V_g$ curves. The change in the surface potential with respect to the pH 7.4 solution, set at zero, was plotted *versus* pH for three nanowires and three nanoplates and is shown in Figure 4. We achieve a 55.8 mV/pH sensitivity for the nanowires and 51.0 mV sensitivity for the nanoplates, with the Nernstian limit being 59 mV/pH. The sensitivity of nanowires being higher than nanoplates or microwires agrees well with literature,[16,40,63] as does the range of pH sensitivities found for the $HfO_2$ sensing dielectric. Our numerical simulations that applied a self-consistent solution of Poisson−Boltzmann electrostatics coupled with OH functional group site-binding model (see Materials and Methods section for details) reproduces key experimental trends (line fit in Figure 4B). Specifically, the model predicts a pH sensitivity of 51 mV/pH, which is very close to the experimental results.

The sensing of the DNA target was done with different molecular weight PLL functionalizations using the same probe molecule. The procedure for modifying the surface is explained in detail in the Materials and Methods section but outlined in Figure 5A. Briefly, the poly-L-lysine is electrostatically adsorbed onto the $HfO_2$ surface and baked on a hot plate at 85 °C to ensure a good linkage. Then, the ssDNA probe is electrostatically bound to the $HfO_2$ surface and excess rinsed off. The ssDNA probe is then baked in order to immobilize it to the poly-L-lysine layer. The target is then hybridized with the probe and sensed on the device. Poly-L-lysine was chosen since it can be deposited from an aqueous solution and electrostatically bound to both the $HfO_2$ and phosphate backbone of probe DNA. This allows for the probe DNA, and binding target, to be in a horizontal conformation.[64] As opposed to a vertical conformation, a horizontal conformation allows for charge density to be closer to the surface, thus creating a larger shift in the surface potential. A horizontal conformation allows for more charge to be felt in the channel at a certain Debye length of electrolyte solution. Other conjugation methods, such as using epoxysilanes with amine-modified probes,[65] afforded a lower change in surface potential when depositing the probe in the beginning. The change in surface potential for the probe conjugation was measured both for the epoxysilane and the different molecular weight poly-L-lysines. Both probe conjugations using the different molecular weight

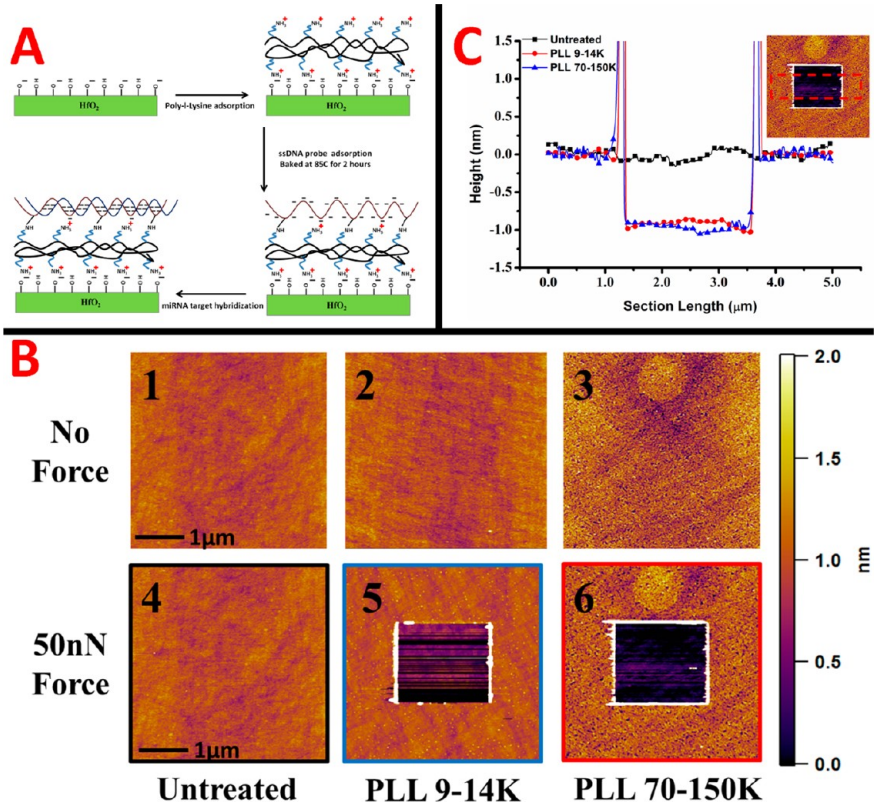


**Figure 5. (A) Schematic of the surface functionalization of the $HfO_2$ surface for microRNA (DNA analogue) sensing. (B) AFM images of the $HfO_2$ and poly-L-lysine layers of different molecular weights. Tapping mode images with no force applied (top) for the different layers and after a 50 nN scratching force (bottom) are displayed. The scale bar for all AFM images is on the right. (C) Cross section for the images with 50 nN force applied. The cross sections are color-coded to images in (B) with the inset representing the cross-sectional area.**

poly-L-lysines gave larger surface potential shifts than for the epoxysilane (Supporting Information Figure S3). Thus, we decided to use and compare the different molecular weight poly-L-lysines for deposition of probes and sensing of target molecules. The sensitivities for the devices with different molecular weight poly-L-lysines are quite different, which we discuss in Figure 7. A lower sensitivity would occur if the overall effective charge density during binding is less or the charges were farther removed from the surface. A few possibilities which would lead to this are the morphology of the polylysine layers as well as the probe density. Thus, we characterized the polylysine layers and probe attachment to understand the underlying reasons for this discrepancy.

We used a combination of ellipsometry, AFM, and XPS to look into the morphology, thickness, and probe densities (Table 1). When the PLL layers were deposited, the ellipsometric thicknesses came out to be within error of each other at ~11 Å each. This indicates the formation of a polylysine monolayer on the surface. The ssDNA probe attachment came out to be within error, as well, at ~20.5 Å each, which leads us to believe the DNA rests in a horizontal configuration. The similar thicknesses for both indicate that we should get similar sensitivity levels for target detection.

Thus, we utilized atomic force microscopy (AFM) to characterize the morphology of the 100 cycle ALD $HfO_2$ layer and the PLL layers. The tapping mode images in Figure 5B are numbered 1−3 in the image set for the untreated $HfO_2$, PLL (9−14K), and PLL (70−150K), respectively. The images for the untreated $HfO_2$ and PLL (9−14K) indicate very smooth and uniform layers. The roughness values extracted for the $HfO_2$ and PLL (9−14K) are 1.1 and 1.6 Å rms, respectively. The morphology of the PLL (70−150K) is much rougher and has a porous, spongelike appearance. These pores, represented by the darker spotted areas in the image, appear to be the thickness of the monolayer or close to it. Moreover, we were able to determine the thickness of the films by applying a 50 nN force to the tip in contact mode and scratching away the PLL layers, then reimaging a larger area in tapping mode. A 50 nN force is known to be more than enough to remove organic monolayers and silane layers, without damaging the underlying surface.[66] The images after a 50 nN force are 4−6 in the image set. The untreated $HfO_2$ shows no changes in height, indicating a hard surface. The PLL layers show distinct changes in thickness, indicated by the square scratched area visualized in images 5 and 6. Taking a section analysis across the scratched areas gives us the thickness of the PLL films and is shown in

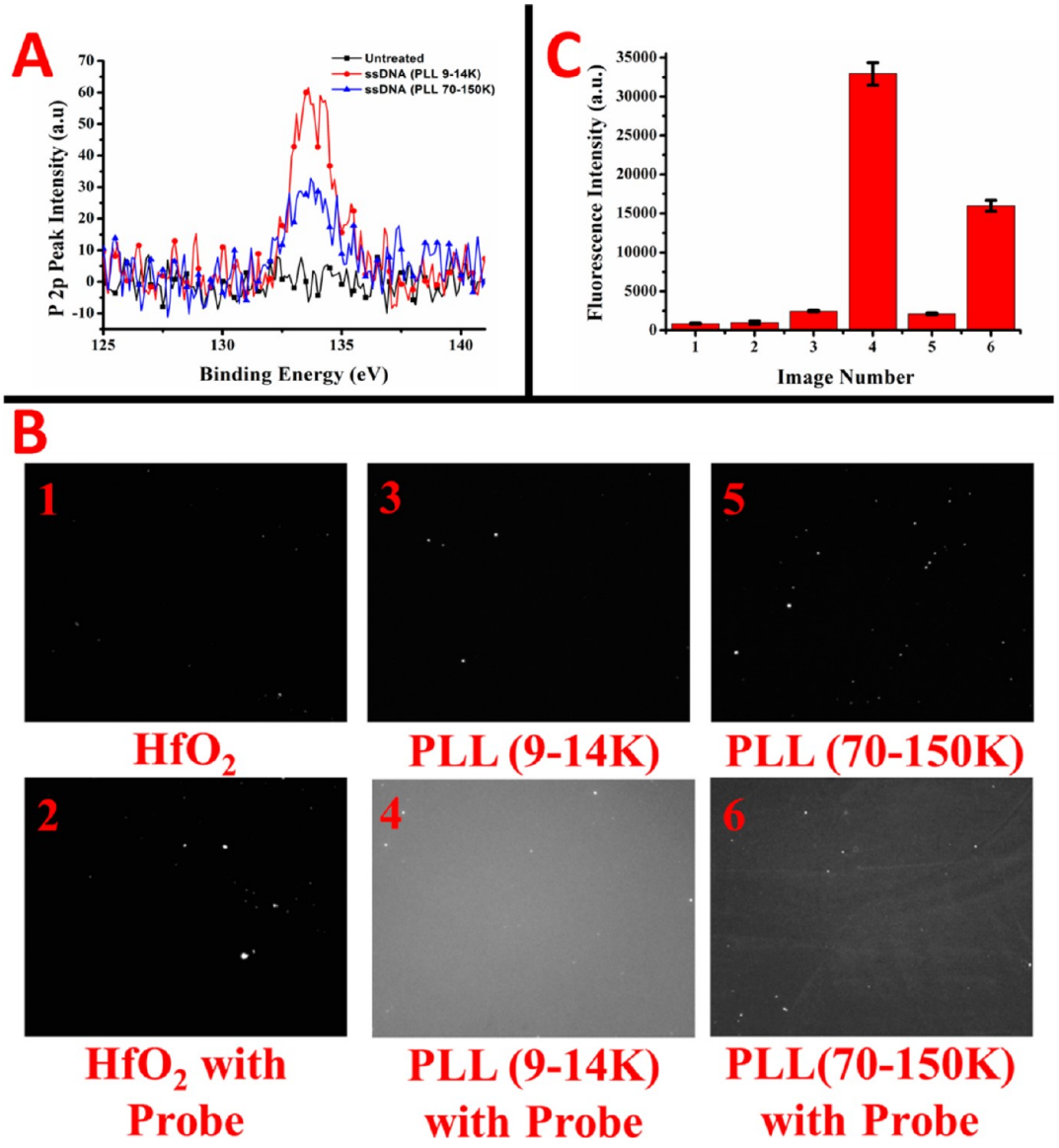


**Figure 6. (A) P2p peak intensities from XPS for ssDNA adsorption onto the poly-L-lysine layers of different molecular weights and onto the bare $HfO_2$ surface. (B) Fluorescent micrographs of ssDNA probe immobilization for $HfO_2$ and the different molecular weight poly-L-lysines, both with and without exposure to ssDNA probe. Fluorescent intensities for images 1–6 in (B) are plotted in column format in (C).**

**TABLE 1. Characterization of the Thickness, Roughness, and Probe Density of the $HfO_2$ Surface Functionalization Process**

| | ellipsometric thickness (Å) | AFM thickness (Å) | roughness (Å) | XPS P2p peak area |
|---|---|---|---|---|
| $HfO_2$ layer | 120.1 ± 3.2 | | 1.1 | |
| PLL 9–14K | 11.3 ± 1.5 | 11.2 | 1.6 | |
| PLL 70–150K | 12.1 ± 2.1 | 9.8 | 3.4 | |
| ssDNA (PLL 9–14K) | 21.6 ± 2.3 | | 1.9 | 145.7 |
| ssDNA (PLL 70–150K) | 19.8 ± 2.7 | | 2.9 | 74.2 |

Figure 5C. The images 4–6 in Figure 5B are color-coded to match up with section analyses in Figure 5C. The section analyses showed a similar thickness for the PLL layers compared to ellipsometry and are in Table 1. However, the buildup of material on the side of the scratched away area was much greater for the lower molecular weight layer (data not shown). This indicates that the amount of material for the higher molecular weight PLL on the substrate was less, leaning toward the evidence of a more porous and incomplete layer.

Attachment of the probe DNA to the PLL layers was measured using two techniques: (1) XPS for the P2p peak intensity from the DNA backbone and (2) fluorescence with a Texas Red labeled miR-10b probe. The

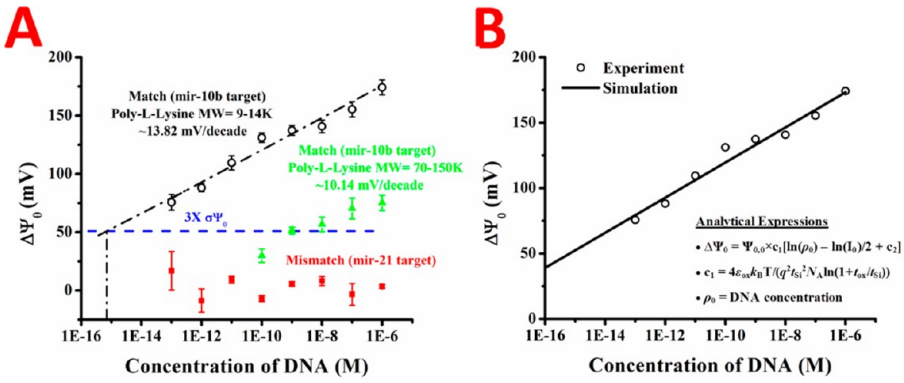


**Figure 7. (A) Change in surface potential *versus* the concentration of target in solution for the two different poly-L-lysines, with the slopes of the respective lines calculated. The change in surface potential for the mismatched target is shown to be negligible (red squares), and a theoretical limit of detection line is drawn in blue. The linear regression for the PLL (9−14K) is shown in (A) (black dashed line) and extrapolated to the theoretical limit of detection line. The change in surface potential *versus* the DNA concentration for the PLL (9−14K) data was also theoretically calculated, and is shown in (B). The change in the surface potential (black circles) matches the theoretical prediction (black line) well. The analytical expressions used for the calculation are shown in the inset in (B). The parameters used in the theoretical calculation of $\Delta\Psi_0$ are $t_{Si}$ = 55 nm, $t_{ox}$(EOT) = 4.22 nm, $N_A = 10^{15}$ cm$^{-3}$, and $I_0$ = 3 mM. The device specific parameters are $\Psi_{0,0}$ = 58.3 mV and $c_2$ = 40.63.**

XPS P2p signal intensity for the $HfO_2$ and probe DNA on the two PLL layers is in Figure 6A. The peak for the ssDNA on PLL(9−14K) is much larger than the one on PLL (70−150k), indicating a higher probe density. The peak intensities are in Table 1, with a ratio of approximately 1.8:1 for the PLL(9−14K)/PLL(70−150K). The fluorescently labeled micrographs of bare $HfO_2$ and PLL layers, both with and without probe, are in Figure 6B. The quantification of the fluorescent intensity is in the bar graph in Figure 6C. Images 1 and 2 show the bare $HfO_2$ layer with and without the probe attachment procedure. The amount of background fluorescence for the $HfO_2$ with and without probe is about the same. Thus, DNA has very little nonspecific adsorption to $HfO_2$, which should make for better selectivity and less issues with blocking. Images 3 and 4 show the background fluorescence for the PLL layers. The PLL (9−14K) layer shows slightly higher background, as to be expected since there are more optically active surface groups according to AFM. The images for the attachment of the miR-10b probe DNA show slightly greater than a 2-fold intensity difference between the PLL layers, with PLL (9−14K) containing the higher probe density. This reaffirms the XPS results in Figure 6A, indicating that the probe density is much higher on the lower molecular weight PLL layer.

The demonstration of sensing of miR-10b DNA analogue target on the $HfO_2$ silicon nanowires is in Figure 7, with the DNA probe and target sequences in Table 2. To make sure the devices were being functionalized properly, $I_d-V_g$ curves at key steps during the probe attachment process were taken to examine the changes in threshold voltage (see Supporting Information Figure S2). First, a reference of the bare $HfO_2$ was taken in the 0.02× SSC sensing buffer. The deposition of PLL then shifts the threshold voltage to the left by ~160 mV. The direction of change is proper since the PLL is positively charged and the device operates in accumulation mode, thus creating a more negative threshold to compensate for the positive increase in surface potential. In contrast, when we adsorb the probe DNA, we cause a shift in the opposite direction of ~90 mV relative to the PLL, which is also expected due to the negative charge density of the phosphate backbone (shifts discussed in more detail in Supporting Information Figure S3). Similar experiments monitoring the adsorption of probe DNA have been performed on nanowires with an 8 nm silicon oxide and showed ~250 mV shifts from the reference monolayer potential.[67] Since our EOT is lower, the probe DNA density may currently be much less using this PLL-based layer and has the potential for further optimization. However, the nanowires and nanoplates in this study did have much greater response than micro-FETs with similar EOT.[68]

**TABLE 2. Nucleic Acid Sequences for the Immobilized Probe and DNA Targets**

| | sequence |
|---|---|
| DNA probe | 5′-CACAAATTCGGTTCTACAGGGTA-3′ |
| miR-10b DNA complementary target | 5′-TACCCTGTAGAACCGAATTTGTG-3′ |
| miR-21 DNA noncomplementary target | 5′-TAGCTTATCAGACTGATGTTGA-3′ |

After conjugating the ssDNA probe to the PLL surface, various concentrations of miR-10b target were allowed to interact with the sensor for 30 min (to offer sufficient time for diffusion-limited transport down to 100 fM concentration),[69] then rinsed off, and $I_d-V_g$ curves recorded in the 0.02× SSC sensing buffer. The threshold voltage change with varying target concentrations was then measured relative to the ssDNA probe reference (shown in Figure 7A). The signal-to-noise ratio (SNR) for the measurements was computed and a blue line drawn for 3× SNR, assumed to be the

limit of detection for the device. For the lower molecular weight polylysine, at least 100 fM of miR-10b target was able to be sensed, with an extrapolated limit of detection of 1 fM. However, for the higher molecular weight polylysine, the limit of detection at 3× SNR is close to 1 nM, close to 6 orders of magnitude higher. When the mismatch miR-21 target was allowed to hybridize with the miR-10b probe, the signal was very small and steady from 100 fM all the way to 1 $\mu$M concentrations. Most of the miR-21 signals were close to or between 0 and 5 mV change in signal. Error bars for the standard deviation of sweeps over the measurement are also presented on the graph for each case. Similar to the trend in pH sensitivity, nanoplates showed a lower hybridization signal with the miR-10b probe at the same concentrations (see Supporting Information Figure S4). For example, the maximum shift for the nanoplate for 1 nM DNA concentration with the PLL 9−14K layer was 41 mV, while the same shift for a nanowire was 108 mV. Similar to the nanowires, the nanoplate also showed the same trend of lower sensitivity with the higher MW PLL layer. The 41 mV shift on the microwire mentioned above only afforded a 28 mV shift with the PLL 70−150K layer as the probe layer for conjugation. We also found that the difference in max potential shifts between the nanowires for the two PLL layers was also greater than it was for the nanoplates. These results for biological detection with nanoplates agree well with the surface potential sensitivity trends presented in Figure 4, as well as the sensitivity difference due to the probe conjugation discussed in Figure 6.

An important feature of the DNA detection sensitivity of NW sensor is that it follows the *logarithmic* dependency on the molecular concentration due to screening by the salt (*i.e.*, $\Delta\Psi_0 \sim \ln(\rho_0)$, where $\rho_0$ is the DNA concentration).[70] The black solid line represents the corresponding theoretical estimation of $\Delta\Psi_0 = \Psi_{0,0} \times c_1[\ln(\rho_0) - \ln(l_0)/2 + c_2]$, where $c_1 = 4\varepsilon_{ox}k_BT/(q^2t_{Si}{}^2N_A\ln(1 + t_{ox}/t_{Si}))$, $\Psi_{0,0}$ and $c_2$ are parameters that depend on device properties, pH, and duration of sensing (*e.g.*, 30 min).[65]

The fact that the lower molecular weight PLL shows such higher sensitivity may be attributed to differences in the monolayers. Most important, the overall probe attachment density is much less on the higher molecular weight layer. This will decrease the total amount of binding target, thus causing smaller shifts in surface potential. Moreover, the roughness of the high molecular weight PLL is larger and looks porous compared to the other layer. If the pore sizes are of the width of the nanowires or smaller, this would lead to large void spaces over the nanowire area without probe, making the microscopic amount of probe DNA even less than in the case for a macroscopic image.

## CONCLUSIONS

In this paper, we have presented a process for the fabrication of $HfO_2$-based top-down silicon nanowires and nanoplates with high stability and robustness in fluid. The ALD process for creating the $HfO_2$ gate dielectric was thoroughly characterized by ellipsometry, AFM, and CV measurements to ensure us of a high-quality layer. The devices respond to pH in accordance to sensitivities of other $HfO_2$ ISFETs, with nanowires slightly more sensitive than plates. Moreover, we characterized the difference between different molecular weight layers of PLL in terms of their surface morphology, thickness, and probe attachment densities. The average thicknesses of the layers were found to be about the same by AFM and ellipsometry; however, the probe density of the lower molecular weight PLL was about twice as much as the higher molecular weight one. This was confirmed by both fluorescence and XPS. Moreover, the AFM indicated that the higher molecular weight PLL was much rougher and porous, perhaps contributing to the lower response to DNA target using this polymer. Using these different layers for sensing of single-stranded DNA oligomers on a nanowire yielded limit of detection differences over 5 orders of magnitude, with the lower molecular weight PLL having higher sensitivity. By using the lower molecular weight poly-L-lysine, we were able to detect down to 100 fM of the miR-10b DNA analogue with a theoretical limit of detection of 1 fM.

## MATERIALS AND METHODS

**Materials.** All metals for e-beam evaporation were of 99.999% purity and purchased from Lesker Co. DNA and miDNA strands were purchased from Integrated DNA Technologies and purified using HPLC. Poly-L-lysine (PLL) of MW 9000−14 000 and MW 70 000−150 000 were purchased from Sigma in powder form and used without further purification. Robinson buffer solutions composed of 1 mM acetic acid, 1 mM phosphoric acid, and 1 mM boric acid were titrated with NaOH/HCl from pH values of 4−12. All buffer components were purchased from Fisher Scientific. A leak-free Ag/AgCl reference electrode was used to apply bias to the fluid on top of the devices and was purchased from Warner Instruments.

**Device Fabrication.** A detailed top-down fabrication flow has been described previously for creating similar silicon nanoFET devices.[40] The fabrication flow began with bonded silicon-on-insulator (SOI) wafers, doped p-type at $10^{15}/cm^2$ with a buried oxide thickness of 1450 Å and top silicon thickness of 550 Å. The top silicon was thinned to approximately 300 Å by dry oxidation and stripping of the oxidized layer with 10:1 buffered oxide etch. The wires were then defined *via* electron beam lithography and wet etched with 25% TMAH to define the active silicon area.[16,60] The source and drain regions were doped with boron (doping $10^{19}/cm^3$) by ion implantation and annealed at 1000 °C for 5 min to active the dopants. The wafer was then dipped in 50:1 BOE for 20 s to remove any native oxide and an SC1/SC2

**TABLE 3. Model Equations of ISFET Electrostatics**

| Region | Model Equations | Description of variables |
|---|---|---|
| Electrolyte | Poisson-Boltzmann Equation<br>$-\nabla(\varepsilon_w \nabla\psi) = -2qn_0 \sinh(q(\psi - V_{FG})/k_B T)$ | $n_0$- buffer ion concentration (3mM, corresponding to 0.02X SSC buffer),<br>$V_{FG}$: fluid gate bias |
| | | $k_B$: Boltzmann constant, T-Temperature |
| Gate dielectric-electrolyte interface | Protonation/de-protonation of OH groups<br>$AOH \leftrightarrow AO^- + H_s^+$<br>$AOH_2^+ \leftrightarrow AOH + H_s^+$<br>OH surface density<br>$N_s = [AOH] + [AO^-] + [AOH_2^+]$<br>Reaction constants<br>$K_a = \frac{[AO^-][H_s^+]}{[AOH]}$ $K_b = \frac{[AOH][H_s^+]}{[AOH_2^+]}$<br>Boundary condition<br>$(\varepsilon_{ox} \nabla\psi\|_{0^-}) - (\varepsilon_w \nabla\psi\|_{0^+}) = q([AOH_2^+] - [AO^-])$ | $H_s^+$ - $H^+$ concentration at gate-oxide/electrolyte interface. $H_b^+$: $H^+$ concentration at the bulk electrolyte.<br>$H_s^+ = H_b^+ e^{-\frac{q\psi}{k_B T}}$ $pH = -\log_{10}(H_b^+)$<br>$N_s$ = 8e14 cm$^{-2}$ for $HfO_2$<br>$pK_a = -\log_{10}(K_a)$, $pK_b = -\log_{10}(K_b)$<br>($pK_a$, $pK_b$) = (6, 10) for $HfO_2$<br>$\varepsilon_w = 80\ \varepsilon_0$, |
| Gate dielectric | Poisson Equation<br>$-\nabla(\varepsilon_{ox} \nabla\psi) = 0$<br>(Acceptor like interface traps ($D_{it}$) are assumed at Si/Gate oxide interface. For $SiO_2/HfO_2$ gate oxide stack, a fixed interface charge is assumed.) | $\varepsilon_{ox}$ = 3.9$\varepsilon_0$ ($SiO_2$) or 20.1$\varepsilon_0$ ($HfO_2$)<br>$D_{it}$: interface trap density at Si/Gate dielectric interface ($D_{it}$ ~ 4x10$^{11}$cm$^{-2}$/eV).<br>$Q_F$: fixed charge density at $SiO_2/HfO_2$ interface. |
| Si | Poisson Equation<br>$-\nabla(\varepsilon_{si} \nabla\psi) = q(p - n - N_A)$<br>$p = n_i e^{-q(\psi - \psi_f)/k_B T}$, $n = n_i e^{q(\psi - \psi_f)/k_B T}$ | $\psi$ -electrostatic potential, $\varepsilon_{si} = 11.9\varepsilon_0$, $\varepsilon_0$ dielectric permittivity of vaccum, q-electronic charge, $N_A$-doping of Si (10$^{15}$ cm$^{-3}$), $n_i$ = 10$^{10}$ cm$^{-3}$, $\psi_f$ -Fermi level in Si. |

clean performed. The wafer then underwent a rapid thermal anneal at 1000 °C for 60 s to help densify the native oxide layer. The $HfO_2$ gate dielectric was deposited by ALD at a temperature of 120 °C for 100 cycles. Following the gate dielectric formation, via holes were etched into the contact regions with 10:1 BOE, and a 100 Å Ni/50 Å TiN layer was deposited in the contact regions by RF sputtering. A rapid thermal anneal was performed at 500 °C in Ar to form NiSi and reduce the contact resistance at the source and drain regions of the devices, while also densifying the $HfO_2$ and creating a wet etch stop. Next, 150 nm of Al was sputtered and patterned over the contact areas. A 450 °C furnace anneal in Ar/$H_2$ was performed for 30 min to anneal the contacts and remove interface traps in the oxide. Afterward, a 5000 Å thick passivation layer of PECVD SiOxNy was deposited over the entire wafer. Metal pad areas on the outside of the Al leads were defined by optical lithography, and 10:1 BOE was used to etch the passivation layer. Metal pads composed of 50 nm Ti/300 nm Ni/500 nm Au were then deposited by e-beam evaporation. The final passivation layer etchback to release the $HfO_2$ devices was done using 10:1 BOE. Subsequently, the wafer is diced (American Precision Dicing) into chips of 1.5 × 1.5 cm for testing.

**Materials and Device Characterization.** Scanning electron micrographs were taken with a Hitachi S-4800 SEM using secondary electron imaging and an accelerating voltage of 10 kV. Before imaging, the samples were sputtered with Au/Pd (80/20)% to minimize charging of the exposed dielectrics and increase topographical contrast. For thickness characterization, $HfO_2$ of varying thicknesses was deposited by ALD onto polished Si wafers and annealed according to the device fabrication above. The wafer was then covered with photoresist and diced into 1 × 1 cm dyes. Ellipsometry measurements were taken using a Rudolph FEIII ellipsometer at a wavelength of 632.8 nm and an angle of 70°. Each measurement was taken over 10 different areas of a chip and averaged together to get a thickness and standard deviation. For fluorescence measurements, a 1 $\mu$m thick thermal oxide was grown on a polished Si and then 100 cycles ALD $HfO_2$ deposited on top. The thick oxide was grown in order to limit signal degradation due to fluorescence interference contrast (FLIC).[71] Briefly, FLIC occurs when a fluorophore is in close contact to a reflecting surface (*i.e.*, silicon), and the reflected wavelengths from excitation interact with the emission of the fluorophore, altering its intensity to the detector. To ensure excitation of the fluorophores where the emission will not be largely affected, an oxide greater than the excitation wavelength (for Texas Red, 560−580 nm) should be chosen, making 1 $\mu$m of thermal oxide sufficient. The $HfO_2$ was subsequently annealed according to the device fabrication above. Fluorescent images were taken with a Nikon microscope at an exposure of 800 ms and a gain of 1.3×. Atomic force microscopy images of the $HfO_2$ and PLL layers were taken with an Asylum Cypher AFM using a force modulation AFM probe tip (Budget Sensors) with a resonant frequency of 75 kHz and a force constant of 1−3 N/m. Force applied to the substrates during contact mode was calibrated by taking the inverse optical lever sensitivity (invOLS) of the cantilever deflection on a bare $HfO_2$ surface and calculating the spring constant of the cantilever by fitting the thermal fluctuations. X-ray photoelectron spectroscopy of the $HfO_2$, DNA, and PLL layers was taken with a KRATOS Axis Ultra XPS at a takeoff angle of 90°. Survey spectra were acquired at a pass energy of 160 eV with 2 sweeps collected.

**TABLE 4. Model Equations for Noise Estimation**

| Region | Model Equations | Description of Variables |
|---|---|---|
| Si-NW | Low-frequency voltage noise<br>$\delta V_{1/f} = \sqrt{\int_{f_1}^{f_2} S_{V_{FB}} df} = \sqrt{\frac{q^2 k_B T N_t \lambda}{WLC_{eff}^2} \ln \frac{f_2}{f_1}}$<br>where $S_{V_{FB}} = \frac{q^2 k_B T N_t \lambda}{fWLC_{eff}^2}$<br>(Acceptor like interface traps ($D_{it}$) are assumed at Si/Gate oxide interface. For $SiO_2/HfO_2$ gate oxide stack, a fixed interface charge is assumed.) | $W = 0.1\,\mu$m, $L = 20\,\mu$m<br>$f_1 = 1$Hz, $f_2 = 1$kHz ($f_1$, $f_2$: low and high cutoff frequency)<br>$\alpha = 1.5\times10^5$ V s/C (Coulomb scattering coefficient)<br>$\lambda = 0.5$ Å (tunneling parameter)<br>$N_t = 3\times10^{16}$ eV$^{-1}$ cm$^{-3}$, (trap density)<br>$C_{eff} = (1/C_{SiO2}+1/C_{HfO2})^{-1} = 8.17\times10^{-7}$ F/cm$^2$<br>$T$=300K |
| Electrolyte | Electrolyte bulk resistance<br>$\delta V_e = \sqrt{\int_{f_1}^{f_2} S_{V_e} df} = \sqrt{4k_B T R_b (f_2 - f_1)}$<br>where $S_{V_e} = 4k_B T R_b$ s and $R_b \simeq \sqrt{\pi / WL}/\kappa$ | $\kappa = 0.124\times10^{-3}$ S/cm (electrolyte conductivity),<br>$k_B$: Boltzmann constant, T-Temperature |

High-resolution spectra of Hf4f, P2p, O1s, C1s, and N1s peaks were collected at a pass energy of 40 eV with a total of 25 passes per peak.

**Electrical Measurements.** High-frequency $C-V$ measurements of $HfO_2$ MOS capacitors were performed at 1 MHz using a Keithley semiconductor parameter analyzer (Keithley 4200) and corrected for series resistance. The capacitors had a top contact of 30 nm TiN/100 nm Al and a back contact of 100 nm Al, which were DC sputtered. Electrical current measurements and applied biases were controlled by the Keithley 4200, as well. Fluid gate biases were applied with a leak-free Ag/AgCl reference electrode (Warner Instruments) that made contact to the solution. Back gate biases were applied using the conductive platform of the probing station which made contact to the backside of the FET dyes. At any other times, the conductive platform served as the ground for the FET dyes while biases were applied to the fluid gate electrode. The Robinson buffer pH solutions were made using 1 mM acetic, 1 mM phosphoric, and 1 mM boric acid with titrated HCl/NaOH to obtain the desired pH. All pH solutions were measured at the conclusion of the experiment to ensure that the pH had not changed significantly during the course of the experiment.

**Preparation of Devices for DNA Sensing.** Before depositing poly-L-lysine, chips were degreased with acetone and methanol, then rinsed in DI water for 1 min. The chips then underwent an $O_2$ plasma at 500 mTorr and 200 W for 5 min. Poly-L-lysine solutions were made to 0.2 mg/mL concentration in 5 mM $Na_2B_4O_7$, pH 8.5. These conditions were chosen since similar depositions have yielded monolayers for lower MW polymers.[72] Chips are soaked in PLL solution for 2 h, then taken out of the solution and rinsed in DI water for 1 min. Chips are then blown dry with $N_2$ and desiccated for 10 min. The chips are baked at 85 °C in a vacuum oven for 4 h afterward.

DNA probe and targets were obtained from Integrated DNA Technologies and diluted to a stock concentration of 100 $\mu$M in DI water. All stock solutions were stored at −20 °C until used. DNA probe solution (10 $\mu$M in 3× SSC buffer) was spotted on the device in a 10 $\mu$L volume and allowed to sit for 2 h in a humidity chamber. The chip was then rinsed in 2× SSC, 0.2× SSC, and 5% EtOH for 1 min each, and blown dry with $N_2$. To cross-link the DNA to the PLL, chips were baked at 85 °C for 2 h in a convection oven. A PDMS well with an adhesive bottom tape was attached to the chip afterward. Each well had a circular diameter of 5 mm and a fluid volume of ~50 $\mu$L. The target solutions for varying concentrations of miR-10b and miR-21 were made in 2× SSC buffer and put in the PDMS well for 30 min to hybridize. The target was then rinsed off three times in 2× SSC buffer and three times in 0.2× SSC buffer before measuring in 0.02× SSC buffer.

**Theoretical Model for pH Response and Noise of SiNW Sensor.** The sensitivity of ISFET to pH fluctuations in the buffer is determined by the protonation/deprotonation kinetics of −OH functional groups at the gate oxide−electrolyte interface and the electrostatics of the system,[5,73,74] as described by the equations in Table 3. For reaction kinetics of −OH functional groups, we use the site binding model[75] with reasonably calibrated parameters ($N_s$, $K_a$, and $pK_b$ in Table 3) regarding $HfO_2$ surface due to unavailability of experimentally observed values in the literature. The electrostatics for the rest of the system (electrolyte, gate oxide, and Si) follows the Poisson−Boltzmann equations with given concentration, dielectric constant, and boundary conditions. The model equations in Table 3 are discretized using a finite difference scheme and self-consistently solved using Newton iteration due to the strong nonlinear nature of the equations.[76] For the relevant device dimensions used in our experiments ($t_{Si} \sim 55$ nm, $t_{ox} \sim 4$ nm), the cylindrical gate oxide capacitance, $C_{cylind} = 2\varepsilon_{ox}/(t_{Si} \times \ln(1 + 2t_{ox}/t_{Si}))$ is comparable to the corresponding planar gate oxide capacitance, $C_{cylind} = \varepsilon_{ox}/t_{ox}$. This allows us to reduce the computational complexity and solve the system of equations for the equivalent planar system. We assume Boltzmann distribution for the ions in the electrolyte and long channel with small drain bias to simply estimate the conductance of Si channel.

For the theoretical estimation of voltage noise in ISFET, we consider two major sources of noise: low-frequency $1/f$ noise ($\delta V_{1/f}$) and the electrolyte noise ($\delta V_e$), as summarized in Table 4.[77] Each noise term is obtained by integrating the corresponding power spectral density ($S_{V_{FB}}$ for $1/f$ noise and $S_{V_e}$ for electrolyte noise) in a given frequency range ($f_1 < f < f_2$). We assume the noise sources are uncorrelated, thus the total noise of ISFET pH sensor (illustrated as the horizontal dashed line in Figure 3C) is given by $\delta V = (\delta V_{1/f}^2 + \delta V_e^2)^{1/2}$.

*Conflict of Interest:* The authors declare no competing financial interest.

*Acknowledgment.* We would like to acknowledge the use of the Micro and Nanotechnology Laboratory at UIUC for FET processing, and the Materials Research Laboratory at UIUC for materials characterization. B.R.D. is a trainee supported by the Midwestern Cancer Nanotechnology Training Center (NIH-NCI R25 CA154015) at UIUC. We would also like to acknowledge support from NIH R01-CA20003 and National Science Foundation (NSF) Grant EEC-0425626 (NSF Nanoscale Science and

Engineering Center at Ohio State University). J.-H.G. and M.A.A. acknowledge financial support from MSD Focus Center and computational resources from the Network of computational nanotechnology.

*Supporting Information Available:* The measurement of leakage current through the device to the fluid gate, the transfer curves for the silicon nanowire functionalization process with PLL and probe molecules, changes in surface potential for the different functionalization chemistries for nanowires and nanoplates, and the surface potential changes to DNA concentration for nanoplates are included. This material is available free of charge *via* the Internet at http://pubs.acs.org.

## REFERENCES AND NOTES


1. Harvey, M. A. Point-of-Care Laboratory Testing in Critical Care. *Am. J. Crit. Care* **1999**, *8*, 72–83.
2. Kilgore, M. L.; Steindel, S. J.; Smith, J. A. Evaluating Stat Testing Options in an Academic Health Center: Therapeutic Turnaround Time and Staff Satisfaction. *Clin. Chem.* **1998**, *44*, 1597–1603.
3. Douketis, J. D. Patient Self-Monitoring of Oral Anticoagulant Therapy: Potential Benefits and Implications for Clinical Practice. *Am. J. Cardiovasc. Drugs* **2001**, *1*, 245–251.
4. Price, C. P. Regular Review: Point of Care Testing. *Br. Med. J.* **2001**, *322*, 1285–1288.
5. Bergveld, P. Thirty Years of Isfetology: What Happened in the Past 30 Years and What May Happen in the Next 30 Years. *Sens. Actuators, B* **2003**, *88*, 1–20.
6. Kimura, J.; Kuriyama, T. FET Biosensors. *J. Biotechnol.* **1990**, *15*, 239–254.
7. Lee, C. S.; Kyu Kim, S.; Kim, M. Ion-Sensitive Field-Effect Transistor for Biological Sensing. *Sensors* **2009**, *9*, 7111–7131.
8. Sandifer, J. R.; Voycheck, J. J. A Review of Biosensor and Industrial Applications of pH-Isfets and an Evaluation of Honeywell's "Durafet". *Mikrochim. Acta* **1999**, *131*, 91–98.
9. Schöning, M. J.; Poghossian, A. Bio FEDs (Field-Effect Devices): State-of-the-Art and New Directions. *Electroanalysis* **2006**, *18*, 1893–1900.
10. Yuqing, M.; Jianguo, G.; Jianrong, C. Ion Sensitive Field Effect Transducer-Based Biosensors. *Biotechnol. Adv.* **2003**, *21*, 527–534.
11. Patolsky, F.; Zheng, G. F.; Lieber, C. M. Fabrication of Silicon Nanowire Devices for Ultrasensitive, Label-Free, Real-Time Detection of Biological and Chemical Species. *Nat. Protoc.* **2006**, *1*, 1711–1724.
12. Zheng, G. F.; Patolsky, F.; Cui, Y.; Wang, W. U.; Lieber, C. M. Multiplexed Electrical Detection of Cancer Markers with Nanowire Sensor Arrays. *Nat. Biotechnol.* **2005**, *23*, 1294–1301.
13. Cui, Y.; Wei, Q. Q.; Park, H. K.; Lieber, C. M. Nanowire Nanosensors for Highly Sensitive and Selective Detection of Biological and Chemical Species. *Science* **2001**, *293*, 1289–1292.
14. Stern, E.; Vacic, A.; Rajan, N. K.; Criscione, J. M.; Park, J.; Ilic, B. R.; Mooney, D. J.; Reed, M. A.; Fahmy, T. M. Label-Free Biomarker Detection from Whole Blood. *Nat. Nanotechnol.* **2010**, *5*, 138–142.
15. Stern, E.; Vacic, A.; Li, C.; Ishikawa, F. N.; Zhou, C. W.; Reed, M. A.; Fahmy, T. M. A Nanoelectronic Enzyme-Linked Immunosorbent Assay for Detection of Proteins in Physiological Solutions. *Small* **2010**, *6*, 232–238.
16. Stern, E.; Klemic, J. F.; Routenberg, D. A.; Wyrembak, P. N.; Turner-Evans, D. B.; Hamilton, A. D.; LaVan, D. A.; Fahmy, T. M.; Reed, M. A. Label-Free Immunodetection with CMOS-Compatible Semiconducting Nanowires. *Nature* **2007**, *445*, 519–522.
17. Li, Z.; Chen, Y.; Li, X.; Kamins, T. I.; Nauka, K.; Williams, R. S. Sequence-Specific Label-Free DNA Sensors Based on Silicon Nanowires. *Nano Lett.* **2004**, *4*, 245–247.
18. Hahm, J.; Lieber, C. M. Direct Ultrasensitive Electrical Detection of DNA and DNA Sequence Variations Using Nanowire Nanosensors. *Nano Lett.* **2004**, *4*, 51–54.
19. Fritz, J.; Cooper, E. B.; Gaudet, S.; Sorger, P. K.; Manalis, S. R. Electronic Detection of DNA by Its Intrinsic Molecular Charge. *Proc. Natl. Acad. Sci. U.S.A.* **2002**, *99*, 14142–14146.
20. Gao, A.; Lu, N.; Dai, P.; Li, T.; Pei, H.; Gao, X.; Gong, Y.; Wang, Y.; Fan, C. Silicon-Nanowire-Based CMOS-Compatible Field-Effect Transistor Nanosensors for Ultrasensitive Electrical Detection of Nucleic Acids. *Nano Lett.* **2011**, *11*, 3974–3978.
21. Zhang, G. J.; Chua, J. H.; Chee, R. E.; Agarwal, A.; Wong, S. M. Label-Free Direct Detection of MiRNAs with Silicon Nanowire Biosensors. *Biosens. Bioelectron.* **2009**, *24*, 2504–2508.
22. Luo, L.; Jie, J.; Zhang, W.; He, Z.; Wang, J.; Yuan, G.; Wu, L. C. M.; Lee, S. T. Silicon Nanowire Sensors for $Hg^{2+}$ and $Cd^{2+}$ Ions. *Appl. Phys. Lett.* **2009**, 94.
23. Wang, W. U.; Chen, C.; Lin, K. H.; Fang, Y.; Lieber, C. M. Label-Free Detection of Small-Molecule−Protein Interactions by Using Nanowire Nanosensors. *Proc. Natl. Acad. Sci. U.S.A.* **2005**, *102*, 3208–3212.
24. Elibol, O. H.; Morisette, D.; Akin, D.; Denton, J. P.; Bashir, R. Integrated Nanoscale Silicon Sensors Using Top-Down Fabrication. *Appl. Phys. Lett.* **2003**, *83*, 4613–4615.
25. Kim, A.; Ah, C. S.; Yu, H. Y.; Yang, J. H.; Baek, I. B.; Ahn, C. G.; Park, C. W.; Jun, M. S.; Lee, S. Ultrasensitive, Label-Free, and Real-Time Immunodetection Using Silicon Field-Effect Transistors. *Appl. Phys. Lett.* **2007**, 91.
26. Choi, S.; Park, I.; Hao, Z.; Holman, H. Y. N.; Pisano, A. P. Quantitative Studies of Long-Term Stable, Top-Down Fabricated Silicon Nanowire Ph Sensors. *Appl. Phys. A: Mater. Sci. Process.* **2012**, 1–8.
27. Ginet, P.; Akiyama, S.; Takama, N.; Fujita, H.; Kim, B. CMOS-Compatible Fabrication of Top-Gated Field-Effect Transistor Silicon Nanowire-Based Biosensors. *J. Micromech. Microeng.* **2011**, 21.
28. Park, I.; Li, Z.; Pisano, A. P.; Williams, R. S. Top-Down Fabricated Silicon Nanowire Sensors for Real-Time Chemical Detection. *Nanotechnology* **2010**, 21.
29. Tong, H. D.; Chen, S.; Van Der Wiel, W. G.; Carlen, E. T.; Van Berg, A. D. Novel Top-Down Wafer-Scale Fabrication of Single Crystal Silicon Nanowires. *Nano Lett.* **2009**, *9*, 1015–1022.
30. Chen, S.; Bomer, J. G.; Van der Wiel, W. G.; Carlen, E. T.; Van Den Berg, A. Top-Down Fabrication of Sub-30 nm Monocrystalline Silicon Nanowires Using Conventional Microfabrication. *ACS Nano* **2009**, *3*, 3485–3492.
31. Chen, S.; Nyholm, L.; Jokilaakso, N.; Karlstrm, A. E.; Linnros, J.; Smith, U.; Zhang, S. L. Current Instability for Silicon Nanowire Field-Effect Sensors Operating in Electrolyte with Platinum Gate Electrodes. *Electrochem. Solid-State Lett.* **2011**, *14*, J34–J37.
32. Kim, S.; Kim, K.; Rim, T.; Park, C.; Cho, D.; Baek, C. K.; Jeong, Y. H.; Meyyappan, M.; Lee, J. S. In *pH Sensing and Noise Characteristics of Si Nanowire Ion-Sensitive Field E□ect Transistors*; 2011 IEEE International Conference on Nano/Micro Engineered and Molecular Systems (NEMS), 2011; pp 1233−1236.
33. Lu, M. P.; Hsiao, C. Y.; Lai, W. T.; Yang, Y. S. Probing the Sensitivity of Nanowire-Based Biosensors Using Liquid-Gating. *Nanotechnology* **2010**, 21.
34. Rajan, N. K.; Routenberg, D. A.; Chen, J.; Reed, M. A. Temperature Dependence of 1/*f* Noise Mechanisms in Silicon Nanowire Biochemical Field Effect Transistors. *Appl. Phys. Lett.* **2010**, *97*, 243501.
35. Zemel, J. N. Microfabricated Nonoptical Chemical Sensors. *Rev. Sci. Instrum.* **1990**, *61*, 1579–1606.
36. Bousse, L.; Bergveld, P. The Role of Buried OH Sites in the Response Mechanism of Inorganic-Gate pH-Sensitive Isfets. *Sens. Actuators* **1984**, *6*, 65–78.
37. Chen, S.; Bomer, J. G.; Carlen, E. T.; Van Den Berg, A. $Al_2O_3$/Silicon Nanoisfet with near Ideal Nernstian Response. *Nano Lett.* **2011**, *11*, 2334–2341.
38. Zafar, S.; D'Emic, C.; Afzali, A.; Fletcher, B.; Zhu, Y.; Ning, T. Optimization of Ph Sensing Using Silicon Nanowire Field Effect Transistors with $HfO_2$ as the Sensing Surface. *Nanotechnology* **2011**, 22.
39. Rothberg, J. M.; Hinz, W.; Rearick, T. M.; Schultz, J.; Mileski, W.; Davey, M.; Leamon, J. H.; Johnson, K.; Milgrew, M. J.;

Edwards, M.; *et al.* An Integrated Semiconductor Device Enabling Non-Optical Genome Sequencing. *Nature* **2011**, *475*, 348–352.
40. Reddy, B., Jr.; Dorvel, B. R.; Go, J.; Nair, P. R.; Elibol, O. H.; Credo, G. M.; Daniels, J. S.; Chow, E. K. C.; Su, X.; Varma, M.; *et al.* High-k Dielectric $Al_2O_3$ Nanowire and Nanoplate Field Effect Sensors for Improved pH Sensing. *Biomed. Microdevices* **2011**, *13*, 335–344.
41. Robertson, J. High Dielectric Constant Oxides. *Eur. Phys. J.* **2004**, *28*, 265–291.
42. Lai, C. S.; Yang, C. M.; Lu, T. F. pH Sensitivity Improvement on 8 nm Thick Hafnium Oxide by Post Deposition Annealing. *Electrochem. Solid-State Lett.* **2006**, *9*, G90–G92.
43. Van Der Wal, P. D.; Briand, D.; Mondin, G.; Jenny, S.; Jeanneret, S.; Millon, C.; Roussel, H.; Dubourdieu, C.; De Rooij, N. F. *High-k Dielectrics for Use as Isfet Gate Oxides*; 2004 Proceedings of IEEE, Sensors, 2004; pp 677−680.
44. Chen, Y. W.; Liu, M.; Kaneko, T.; McIntyre, P. C. Atomic Layer Deposited Hafnium Oxide Gate Dielectrics for Charge-Based Biosensors. *Electrochem. Solid-State Lett.* **2010**, *13*, G29–G32.
45. Gabriely, G.; Teplyuk, N. M.; Krichevsky, A. M. Context Effect: MicroRNA-10b in Cancer Cell Proliferation, Spread and Death. *Autophagy* **2011**, *7*, 1384–1386.
46. Iyevleva, A. G.; Kuligina, E. S.; Mitiushkina, N. V.; Togo, A. V.; Miki, Y.; Imyanitov, E. N. High Level of Mir-21, Mir-10b, and Mir-31 Expression in Bilateral *vs.* Unilateral Breast Carcinomas. *Breast Cancer Res. Treat.* **2012**, *131*, 1049–1059.
47. Ma, L.; Reinhardt, F.; Pan, E.; Soutschek, J.; Bhat, B.; Marcusson, E. G.; Teruya-Feldstein, J.; Bell, G. W.; Weinberg, R. A. Therapeutic Silencing of Mir-10b Inhibits Metastasis in a Mouse Mammary Tumor Model. *Nat. Biotechnol.* **2010**, *28*, 341–347.
48. Ma, L.; Teruya-Feldstein, J.; Weinberg, R. A. Tumour Invasion and Metastasis Initiated by MicroRNA-10b in Breast Cancer. *Nature* **2007**, *449*, 682–688.
49. Cissell, K. A.; Rahimi, Y.; Shrestha, S.; Hunt, E. A.; Deo, S. K. Bioluminescence-Based Detection of MicroRNA, Mir21 in Breast Cancer Cells. *Anal. Chem.* **2008**, *80*, 2319–2325.
50. Liang, Y.; Ridzon, D.; Wong, L.; Chen, C. Characterization of Microrna Expression Profiles in Normal Human Tissues. *BMC Genomics* **2007**, 8.
51. Hausmann, D. M.; Kim, E.; Becker, J.; Gordon, R. G. Atomic Layer Deposition of Hafnium and Zirconium Oxides Using Metal Amide Precursors. *Chem. Mater.* **2002**, *14*, 4350–4358.
52. Kukli, K.; Ritala, M.; Sajavaara, T.; Keinonen, J.; Leskelä, M. Atomic Layer Deposition of Hafnium Dioxide Films from Hafnium Tetrakis(ethylmethylamide) and Water. *Chem. Vap. Deposition* **2002**, *8*, 199–204.
53. Bohra, F.; Jiang, B.; Zuo, J. M. Textured Crystallization of Ultrathin Hafnium Oxide Films on Silicon Substrate. *Appl. Phys. Lett.* **2007**, 90.
54. Wilk, G. D.; Wallace, R. M.; Anthony, J. M. Hafnium and Zirconium Silicates for Advanced Gate Dielectrics. *J. Appl. Phys.* **2000**, *87*, 484–492.
55. Nicollian, E. H.; Brews, J. R. *MOS Physics and Technology*; Wiley: New York, 1982.
56. Callegari, A.; Cartier, E.; Gribelyuk, M.; Okorn-Schmidt, H. F.; Zabel, T. Physical and Electrical Characterization of Hafnium Oxide and Hafnium Silicate Sputtered Films. *J. Appl. Phys.* **2001**, *90*, 6466–6475.
57. Zhong, L.; Daniel, W. L.; Zhang, Z.; Campbell, S. A.; Gladfelter, W. L. Atomic Layer Deposition, Characterization, and Dielectric Properties of $HfO_2/SiO_2$ Nanolaminates and Comparisons with Their Homogeneous Mixtures. *Chem. Vap. Deposition* **2006**, *12*, 143–150.
58. Goncharova, L. V.; Dalponte, M.; Feng, T.; Gustafsson, T.; Garfunkel, E.; Lysaght, P. S.; Bersuker, G. Diffusion and Interface Growth in Hafnium Oxide and Silicate Ultrathin Films on Si(001). *Phys. Rev. B: Condens. Matter Mater. Phys.* **2011**, 83.
59. Rudenja, S.; Minko, A.; Buchanan, D. A. Low-Temperature Deposition of Stoichiometric $HfO_2$ on Silicon: Analysis and Quantification of the $HfO_2$/Si Interface from Electrical and XPS Measurements. *Appl. Surf. Sci.* **2010**, *257*, 17–21.
60. Vu, X. T.; Eschermann, J. F.; Stockmann, R.; Ghoshmoulick, R.; Offenhäusser, A.; Ingebrandt, S. Top-Down Processed Silicon Nanowire Transistor Arrays for Biosensing. *Physica Status Solidi A* **2009**, *206*, 426–434.
61. Vu, X. T.; Stockmann, R.; Wolfrum, B.; Offenhäuser, A.; Ingebrandt, S. Fabrication and Application of a Microfluidic-Embedded Silicon Nanowire Biosensor Chip. *Physica Status Solidi A* **2010**, *207*, 850–857.
62. Fleetwood, D. M.; Winokur, P. S.; Reber, R. A., Jr; Meisenheimer, T. L.; Schwank, J. R.; Shaneyfelt, M. R.; Riewe, L. C. Effects of Oxide Traps, Interface Traps, and "Border Traps" on Metal-Oxide-Semiconductor Devices. *J. Appl. Phys.* **1993**, *73*, 5058–5074.
63. Elfström, N.; Juhasz, R.; Sychugov, I.; Engfeldt, T.; Karlström, A. E.; Linnros, J. Surface Charge Sensitivity of Silicon Nanowires: Size Dependence. *Nano Lett.* **2007**, *7*, 2608–2612.
64. Saprigin, A. V.; Thomas, C. W.; Dulcey, C. S.; Patterson, C. H., Jr.; Spector, M. S. Spectroscopic Quantification of Covalently Immobilized Oligonucleotides. *Surf. Interface Anal.* **2005**, *37*, 24–32.
65. Protocol from Schott Nexterion for DNA Microarray Epoxysilane Slide E. http://www.us.schott.com/nexterion/english/download/protocol_slide_e_1_3_us.pdf.
66. Crampton, N.; Bonass, W. A.; Kirkham, J.; Thomson, N. H. Formation of Aminosilane-Functionalized Mica for Atomic Force Microscopy Imaging of DNA. *Langmuir* **2005**, *21*, 7884–7891.
67. Vu, X. T.; GhoshMoulick, R.; Eschermann, J. F.; Stockmann, R.; Offenhäusser, A.; Ingebrandt, S. Fabrication and Application of Silicon Nanowire Transistor Arrays for Biomolecular Detection. *Sens. Actuators, B* **2010**, *144*, 354–360.
68. Ingebrandt, S.; Offenhäusser, A. Label-Free Detection of DNA Using Field-Effect Transistors. *Physica Status Solidi A* **2006**, *203*, 3399–3411.
69. Nair, P. R.; Alam, M. A. Performance Limits of Nanobiosensors. *Appl. Phys. Lett.* **2006**, 88.
70. Nair, P. R.; Alam, M. A. Screening-Limited Response of Nanobiosensors. *Nano Lett.* **2008**, *8*, 1281–1285.
71. Lambacher, A.; Fromherz, P. Fluorescence Interference-Contrast Microscopy on Oxidized Silicon Using a Monomolecular Dye Layer. *Appl. Phys. A: Mater. Sci. Process.* **1996**, *63*, 207–216.
72. Jordan, C. E.; Frey, B. L.; Kornguth, S.; Corn, R. M. Characterization of Poly-L-lysine Adsorption onto Alkanethiol-Modified Gold Surfaces with Polarization-Modulation Fourier Transform Infrared Spectroscopy and Surface Plasmon Resonance Measurements. *Langmuir* **1994**, *10*, 3642–3648.
73. Landheer, D.; McKinnon, W. R.; Aers, G.; Jiang, W.; Deen, M. J.; Shinwari, M. W. Calculation of the Response of Field-Effect Transistors to Charged Biological Molecules. *IEEE Sens. J.* **2007**, *7*, 1233–1241.
74. Landheer, D.; Aers, G.; McKinnon, W. R.; Deen, M. J.; Ranuarez, J. C. Model for the Field Effect from Layers of Biological Macromolecules on the Gates of Metal-Oxide-Semiconductor Transistors. *J. Appl. Phys.* **2005**, 98.
75. Yates, D. E.; Levine, S.; Healy, T. W. Site-Binding Model of the Electrical Double Layer at the Oxide/Water Interface. *J. Chem. Soc., Faraday Trans. 1* **1974**, *70*, 1807–1818.
76. Go, J.; Nair, P. R.; Reddy, B., Jr.; Dorvel, B.; Bashir, R.; Alam, M. A. In Beating the Nernst Limit of 59mV/pH with Double-Gated Nano-Scale Field-Effect Transistors and Its Applications to Ultra-Sensitive DNA Biosensors. *IEEE Electron Devices Lett.* 2010; pp 8.7.1−8.7.4.
77. Deen, M. J.; Shinwari, M. W.; Ranuárez, J. C.; Landheer, D. Noise Considerations in Field-Effect Biosensors. *J. Appl. Phys.* **2006**, 100.